



Ultra-sensitive pressure sensors based on large alveolar deep tooth electrode structures with greatly stretchable oriented fiber membrane

Quan Yue, Songhua Xiao, Zhibin Li, Jing Yang, Bin Chen, Jiansong Feng, Xu Zhang, Qianling Chen, Taihong Wang^{*}

Department of Electrical and Electronic Engineering, Southern University of Science and Technology, Shenzhen, Guangdong 518055, China

ARTICLE INFO

Keywords:

Far-field EHD
Oriented fiber membrane
Electric double layer
Ultra-sensitivity
Capacitive pressure sensors

ABSTRACT

Electrohydrodynamic (EHD) preparation of micro-nano fibers has significant advantages in the application of ultra-sensitive detection. However, far-field EHD always has the problem of jet instability, which limits its further application. In this study, we excellently realize the generated single jet deposition of aligned fibers by constructing auxiliary electric fields and creatively designed an ultra-sensitive structure based on large alveolar deep tooth electrodes with oriented TPU fiber membrane. As the isolation layer, the oriented fiber membrane controls the formation of the electric double layers by adjusting the contact area between the tooth-shaped electrodes and the polyelectrolyte membrane. Meanwhile, with increasing the pressure, the tooth-shaped electrodes with large alveolar depth bring more sidewall surfaces contact and expand the capacitance adjustment range. Therefore, we can continuously adjust the capacitance of the pressure sensor through the oriented fiber membrane to achieve an ultra-broad linear range (1.1–100 kPa) with ultra-high sensitivity of 230 kPa⁻¹.

1. Introduction

Electrohydrodynamic (EHD) technology has incomparable advantages in manufacturing micro-nano fibers, such as simple equipment, low processing cost and easy realization. It is widely used in biomedicine [1–3], filtration purification [4,5], electronics [6–8], catalysis [9–11]. However, the instability [45–47] of the jet during the EHD process makes it difficult to program deposition, resulting in disorderly arranged fibers [48,49], which greatly limits the development and application of this technology.

For a long time, many researches have been devoted to enhancing the stability of EHD jet deposition and different schemes have been proposed. Through the high-speed rotation of special shaped collecting devices such as drum [12,13], disk [14] and cylinder grid [15], the oriented fibers could be obtained. In recent years, the near-field EHD technology becomes widely popular [16–18]. By reducing the distance between the nozzle and the collector, the stable movement area of the jet was used to avoid the instability area, and the controllable deposition of the jet was realized. Yang-Seok Park [8] exhibited a near-field EHD jet to achieve precise stack deposition of fibers by adding NaCl salt to the polymer solution. Although the near-field EHD avoids the jet unsteady motion zone, it loses the space between the nozzle and the collector and

requires high-speed movement of the platform. Donghwi Cho [19] introduced insulating blocks between the nozzle and the collector to control the electric field distribution, realized the alignment of fibers, and prepared parallel, vertical and rhombic structures. Dan Li [20] used two parallel collectors with a certain distance to get aligned fibers. Another improved parallel electrode method [21] was proposed, which controlled the jet by placing a positively charged metal ring between the nozzle and the parallel collection electrodes to prepare aligned composite fibers. Controlled jet deposition can also be achieved by attaching a relatively hydrophobic and insulating substrate to an aluminum foil as a collector [22]. Jongwan Lee [23] placed the grounding pin under the glass collector and the cylindrical side wall electrode between the nozzle and the collector to suppress the instability of the jet and to produce nanofiber patterns. Xiaojie Cui [24] used a metal plate and a metal ring with voltage bias to restrict the diffusion motion of the jet in the EHD device to realize the controllable deposition of fibers. In addition, the electrodes were introduced into the EHD device to construct a variable electric field, and the jet deflected under the action of the electric field force to control the fibers deposition. Christian Grassl [25] proposed that when the voltage with a certain frequency change is applied to the parallel electrodes, the jet will deflect periodically between the electrodes under the action of the electric field force, and the unstable

^{*} Corresponding author.

E-mail address: wangth@sustech.edu.cn (T. Wang).

<https://doi.org/10.1016/j.cej.2022.136370>

Received 22 December 2021; Received in revised form 28 February 2022; Accepted 10 April 2022

Available online 12 April 2022

1385-8947/© 2022 Elsevier B.V. All rights reserved.

motion of the jet will be well restrained. Based on Christian Grassl's [25] research, Liashenko [26] successfully printed the 3D structures with submicron scale by placing electrodes perpendicular to each other combined with near-field EHD method. Rebrov [27] proposed to connect the high voltage pulse generator to the collector and realize the directional deposition of fibers by manipulating the electric field to prepare the oriented fibers in a large area. The previous works on EHD technology have made significant progress, which provides important reference values for this research. However, the instability and controllable deposition of far-field EHD jet has not been effectively solved. With the development of artificial intelligence, sensors are more and more widely used in tactile [50,51] and proximity perception [52]. Improving the sensitivity of capacitive pressure sensors is mainly to make changes to the structure/material of the electrodes and the dielectric layers. Using materials with microstructural features as electrodes, such as metal nanowires [28,29], carbon nanotubes [30,50], and graphene [31], or construct microstructures [32] on the electrode surfaces to improve sensitivity, and ionic gel electrodes [33] are also used to improve sensitivity. It seems more popular to improve sensitivity by designing dielectric layer structure, pyramids [34,44], micropillars [35], sphere microarray [43], porous structure [53] and nanofibrous membrane [36] dielectric layers are widely used.

In this study, we propose the method of constructing auxiliary electric fields to control the generated single jet deposition. By introducing an auxiliary electrode near the nozzle of EHD equipment, the focused electric field was constructed between the nozzle and the collector. It was easy to achieve a single stable jet with a collection distance of 10 cm, which effectively solved the problem of instability of far-field EHD jet. Then, we designed deflection electric field in the device, controlled the single stable charged jet to deflect rapidly under the action of electric field force, deposited regular patterns and prepared oriented fiber membrane. Innovatively, using the controllable far-field EHD technology, we demonstrate an ultra-sensitive structure based on large alveolar deep tooth electrodes with oriented TPU fiber membrane. The oriented fibers were placed between the electrodes and the polyelectrolyte membrane as isolation layers, so that the sensor obtained a small initial capacitance value. The formation of the electric double layers were adjusted through the oriented fiber membrane to control the change of capacitance in a wide range. With the combination of oriented fiber membrane, polyelectrolyte membrane and tooth-shaped electrodes, the pressure sensor shows great advantages in linearity and sensitivity, achieving an ultra-broad linear range (1.1–100 kPa) with ultra-high sensitivity of 230 kPa^{-1} , providing a new idea for ultra-sensitive detection.

2. Experimental section

2.1. Materials

Polyvinylpyrrolidone (PVP, K90) was purchased from Shanghai Aladdin Biochemical Technology Co, Ltd. Thermoplastic polyurethane (TPU-1065A), purchased from DaDong Resin Chemical Co, Ltd. N, N-dimethylformamide (DMF, reagent pure), purchased from Shanghai Macklin Biochemical Technology Co. Ltd. Acetone (Chromatographic reagent) was purchased from XiLong Chemical Co, Ltd. PVDF-HFP was purchased from Sigma Aldrich (Shanghai) Trading Co, Ltd. Lithium bis (trifluoromethanesulfonimide) (LiTFSI, Mw 287.09, purchased from Shanghai Aladdin Biochemical Technology Co, Ltd. Polydimethylsiloxane (PDMS, Dow Corning dc184), purchased from Dow Chemical.

2.2. Equipment

High voltage power supply (DWP-303-1ACD1) was purchased from Tianjin DongWen High Voltage Power Supply Corp. The syringe pump (LSP01-1A) is purchased from Baoding Longer Precision Pump Co., Ltd.

SN60U HD industrial camera was purchased from Shenzhen SangNond Technology Co., Ltd. Microcomputer controlled electronic universal testing machine (LD23.501), purchased from LiShi (Shanghai) Instruments Co., Ltd. LCR Meter (E4980AL), purchased from Keysight Technologies Co., Ltd; High vacuum magnetron sputtering coater (JCP200), purchased from Beijing Technol Science Co., Ltd. Temperature & Humidity Test Chamber, purchased from Dongguan A-Pex Test Equipment Co., Ltd.

2.3. Preparation of solution

2.3.1. Preparation of PVP solution

Weighted different mass (0.8 g, 1.0 g, 1.2 g) of polyvinylpyrrolidone (PVP) powder into 10 ml of absolute ethanol, put the mixed solution on a magnetic stirrer, and stirred for 4 h at room temperature.

2.3.2. Preparation of PDMS solution

PDMS prepolymer and crosslinking agent were mixed in a ratio of 10:1, fully stirred, and then vacuumed to remove bubbles.

2.3.3. Preparation of TPU solution

Weighted 1.8 g thermoplastic polyurethane (TPU) particles, and then added the mixed solvent of DMF and acetone (5 ml DMF, 6.25 ml acetone). At 75 °C, stirred with standard heating magnetic stirrer for 24 h. TPU was fully mixed with DMF and acetone to dissolve.

2.3.4. Preparation of PVDF-HFP solution

Weighted 0.8 g PVDF-HFP, added it into 8 g DMF solvent, stirred for 6 h until dissolved and fully mixed.

2.3.5. Preparation of PVDF-HFP & LiTFSI polyelectrolyte solution

Weighted 0.8 g PVDF-HFP and 0.8 g LiTFSI respectively, added them into 8 g DMF solvent, stirred for 24 h, dissolved and mixed thoroughly. Polyelectrolyte membrane obtained by ordinary EHD method.

2.4. Jet focusing experiment

Set the flow rate to 0.8 ml/h at a collection distance of 7 cm and 0.2 ml/h at a collection distance of 10 cm. The flow rate of the solution is controlled by syringe pump. The diameter of the auxiliary electrode of the metal plate and the metal ring is 10 cm.

2.5. Jet deflection experiment

Two parallel metal plate electrodes are 3 cm in length, 2 cm in width and 0.1 cm in thickness, placed about 5 mm above the collector. In the square wave pattern deposition experiment, the flow rate was set to 0.8 ml/h, and the others were 0.2 ml/h. The solution ratio is 1.0 g PVP/10 ml ethanol. The applied deflection voltage in [Movie S1](#) was about 2.5 kV.

3. Results and discussion

3.1. Jet focusing

In order to solve the problem of EHD jet instability, we have made a lot of efforts. Initially, we set the distance between the nozzle and the collector (collection distance) to 7 cm and the voltage of the nozzle to 5 kV. It can be seen ([Fig. S1, Supporting Information](#)) that compared with no negative high voltage, applying -6 kV high voltage can increase the length of the jet stabilization zone. Before jetting, the fluid contacts with the metal nozzle with 5 kV high voltage, the charge transfer occurs at the contact interface, and the jet is charged after jetting [37]. Therefore, we considered introducing a metal ring auxiliary electrode near the nozzle and applying negative high voltage on the collector to construct a focusing electric field to suppress the unstable motion of the jet ([Fig. S2,](#)

Supporting Information). The metal ring was connected with the positive high voltage power supply, and the length of the stable region and the area of the deposition region of the jet could be controlled by adjusting the power supply voltage. When the applied voltage of the ring is 9 kV, a stable single jet was obtained, and the problem of unstable motion of the jet was well solved. Further, the metal plate could be seen as composed of many metal rings with different diameters. Subsequently, a metal plate auxiliary electrode (Fig. S3, Supporting Information) was introduced near the nozzle, and a single stable jet could also be obtained. In the device, the metal plate auxiliary electrode and the metal nozzle contacted to form an equipotential, and a focusing electric field was formed between the nozzle and the collector, which inhibited the instability of the jet. Adjusting the nozzle voltage to 8 kV and the collecting plate voltage to -9 kV, we could easily achieve single stable jet deposition at the collection distance of 10 cm (schematic diagram of the device is shown in Fig. 1a). The jet kept a single beam from the nozzle to the collector, and there was no divergence and large-scale unstable movement. As shown in the optical images of the single stable jet taken by industrial camera near the nozzle (Fig. 1b) and the collector (Fig. 1c). Moreover, we used COMSOL software to simulate the electric field distribution in the working space of the device, and it is easy to see the focusing effect of the electric field on the charged jet in the upper area of the single stable jet, shown in Fig. 1d. So far, the far-field EHD single stable jet deposition has been realized.

3.2. Jet deflection

The traditional method to obtain oriented fibers needs the high-speed movement of the mechanical device to pull the jet to obtain the straightened fibers [13,16,25]. In this study, the controllable deposition of EHD jet was realized by constructing periodically changing deflection electric field to drive the single stable charged jet. Based on the EHD jet focusing device, two parallel metal plate electrodes were introduced, and the complementary pulse high voltages (deflection voltage U) was applied to electrode A and electrode B respectively, as shown in Fig. 2a. Different from previous study [25], we introduced deflection electric field on the basis of realizing single stable jet in far field (5 cm collection distance) EHD, which could realize more effective control of jet motion. COMSOL simulates the potential distribution (Fig. 2b) and the corresponding optical images of jet deflection (Fig. 2c), with the collection distance of 5 cm, the nozzle voltage of 5 kV, the collector voltage of -4 kV and the deflection voltage of 5 kV. Applying deflection voltage, the generated single stable jet deflected under the action of the periodically changing electric field force, and the collector moved at a speed of 12.5 cm/s, the jet was deposited to form a square wave pattern (Fig. S4, Supporting Information) and the jet deflection process is shown in Movie S1. We prepared polyvinylpyrrolidone (PVP) with different contents (0.8 g, 1.0 g, 1.2 g) in 10 ml ethanol to study the effect of solution

concentration on the diameter of deposited fibers. It can be seen from the SEM images (Fig. S5, Supporting Information) of the deposited fibers that with the increase of PVP content, the obtained fiber diameter gradually increases. Among, the fiber prepared by 0.8 g PVP content solution reaches the smallest diameter of 433 ± 9 nm, reducing the PVP content, the EHD jet was difficult to form, and when the PVP content increases to 1.2 g, the fiber diameter reaches 1223 ± 72 nm (shown in Fig. 2d). Fig. 2e shows the deposition morphologies of the jet on the collector when the deflection voltage was 4 kV, 8 kV and 12 kV respectively, and the deflection voltage switching frequency was 20 Hz. With the increase of deflection voltage, the electric field force on the jet increases and the fiber stretches gradually. When the deflection voltage was 4 kV, the fibers morphology was spiral and when the voltage increased to 12 kV, the fibers were completely stretched straight (Fig. 2e). Also, we used the electric field to control the deposition of single jet to realize the printing of regular checkered patterns. First, deposited a layer of oriented fibers on the collector, and then deposited the second layer of oriented fibers perpendicular to the first layer to form a regular grid pattern, as shown in Fig. 2f. Here, we realized the controllable deposition of far-field EHD jet.

3.3. Preparation and mechanical properties characterization of oriented TPU fibers

Thermoplastic polyurethane (TPU) has good elastic properties and has been used in many fields [38–40]. The research on preparing TPU fibers by EHD method is relatively mature. This section introduces the preparation of oriented TPU fibers and the characterization of mechanical properties of oriented fibers. As shown in Fig. 3a, oriented TPU fibers deposited on two parallel silicon wafers, the diameter of the fibers deposited on the silicon wafer part was about 619 ± 22 nm, and the diameter of the suspended part was smaller, about 498 ± 14 nm. The strain ε of fiber refers to the relative change of fiber deformation, which is expressed by the ratio of deformation to initial value. Fig. 3b shows the fibers were stretched to 100%, 300% and 500% strains respectively and the corresponding optical images of aligned fibers taken by the industrial camera. With the gradual separation of the two silicon wafers, the fibers between the silicon wafers were stretched. From 100% to 500% strain, the fibers can maintain complete morphologies and without fracture, which indicates that the TPU fibers have good tensile properties. The mechanical properties of TPU fiber membrane were tested by computer-controlled electronic universal testing machine. In Fig. 3c, the stress–strain curve of fiber membrane tested at a tensile speed of 20 mm/min and the SEM image of the oriented TPU fiber membrane in the initial state are shown in the inset. The oriented TPU fiber membrane exhibited excellent stretchability, with the strain of up to more than 600% and the maximum tensile strength could reach 5.87 MPa. Fig. 3d shows the load-unload curve of the fiber membrane under

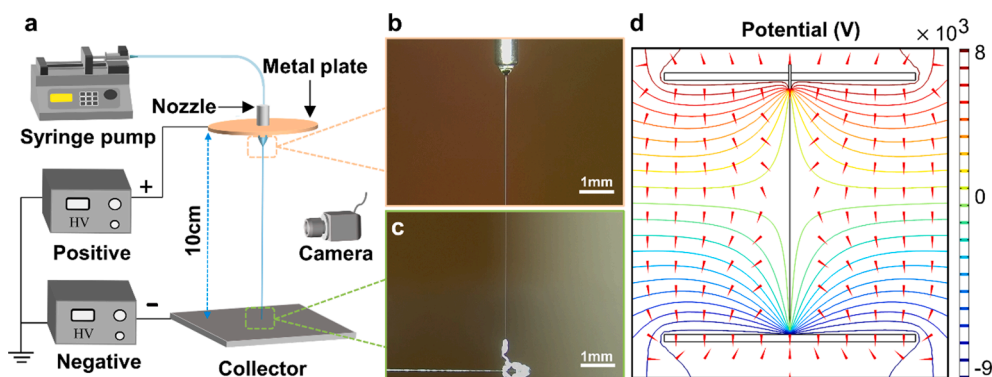


Fig. 1. Jet focusing: (a) Schematic diagram of EHD jet focusing device (10 cm collection distance). Optical images of the single stable jet near the (b) nozzle and (c) collector. (d) COMSOL simulation of the electric field distribution.

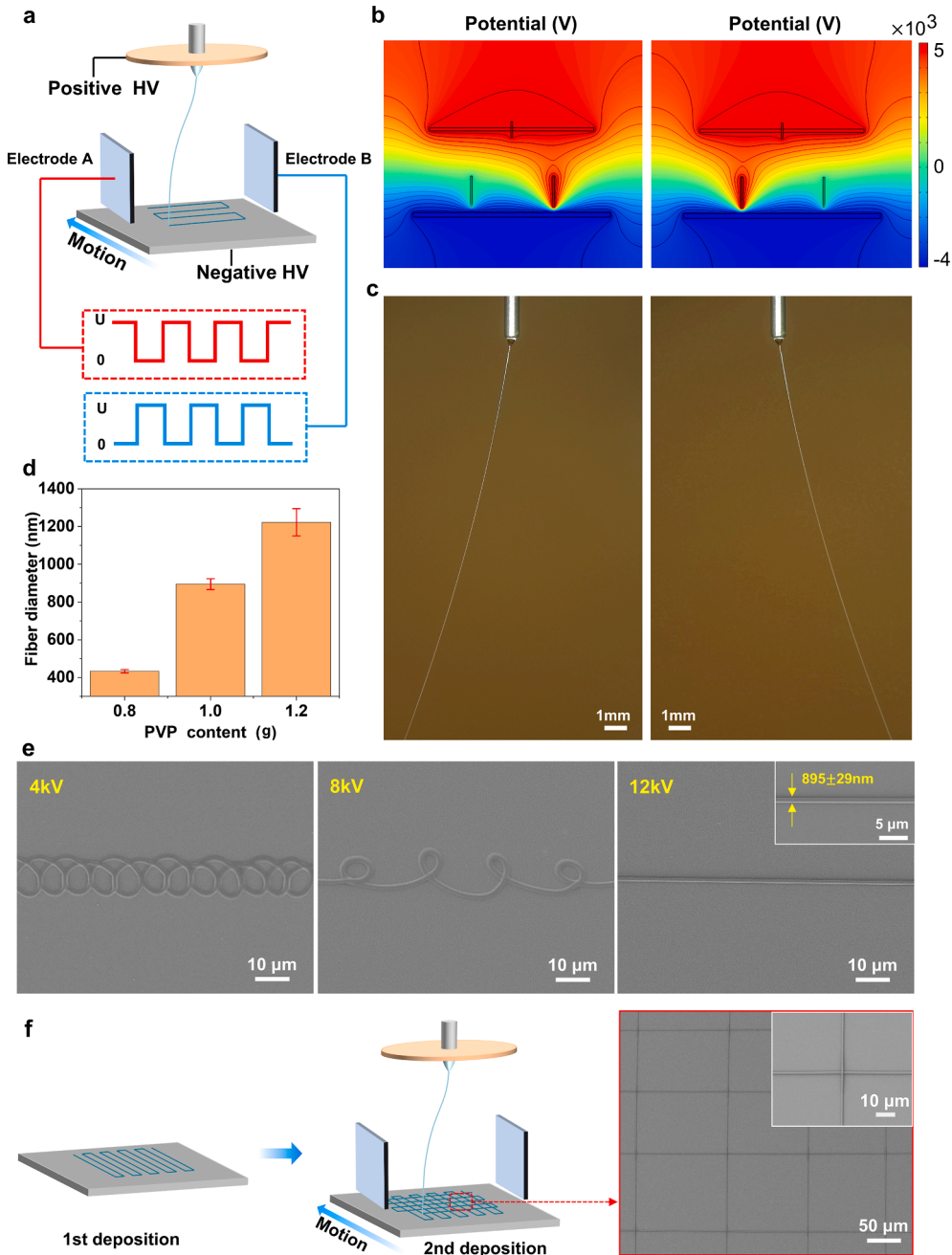


Fig. 2. Jet deflection: (a) Schematic diagram of control jet deflection. (b) COMSOL simulations of the deflection electric field distribution and (c) the corresponding jet deflection optical images. (d) The diameter of deposited fibers with various PVP contents (correspond to Fig. S5, Supporting Information). (e) SEM images of jet deposition morphologies under the deflection voltage of 4 kV, 8 kV and 12 kV respectively. (f) Deposition of regular grid pattern.

300% strain, loading and unloading at a speed of 5 mm/min. It can be seen that the curve of fiber membrane does not coincide during loading and unloading, and there is a gap between the curves, which is due to the energy loss caused by the viscoelasticity of the material during the tensile process of TPU fiber membrane. Additionally, the plastic deformation of the fibers in the tensile process leads to that the end point of the curve does not coincide with the initial point after unloading. Fig. 3e shows the elastic recovery rate and plastic deformation rate of TPU fiber membrane under different strains, the tensile and recovery speed was 5 mm/min.

$$\text{Elastic recovery rate} = \frac{L_1 - L_2}{L_1 - L_0} \quad (1)$$

$$\text{Plastic deformation rate} = \frac{L_2 - L_0}{L_0} \quad (2)$$

where L_0 is the original length, L_1 is the length of elongation under the corresponding strain, and L_2 is the length of the sixth loading to the pretension. As the strain increases, the overall elastic recovery rate shows a decreasing trend. In the strain range of 300% to 400%, the elastic recovery rate gradually increases, which is caused by the calculation method of the elastic recovery rate. During the actual test process, with the increase of strain, the length of the fiber increased, and the plastic deformation rate of the fiber gradually increased, as shown by the red line in Fig. 3e. This part, we have successfully prepared oriented TPU fiber membrane with tensile strain of up to 600%.

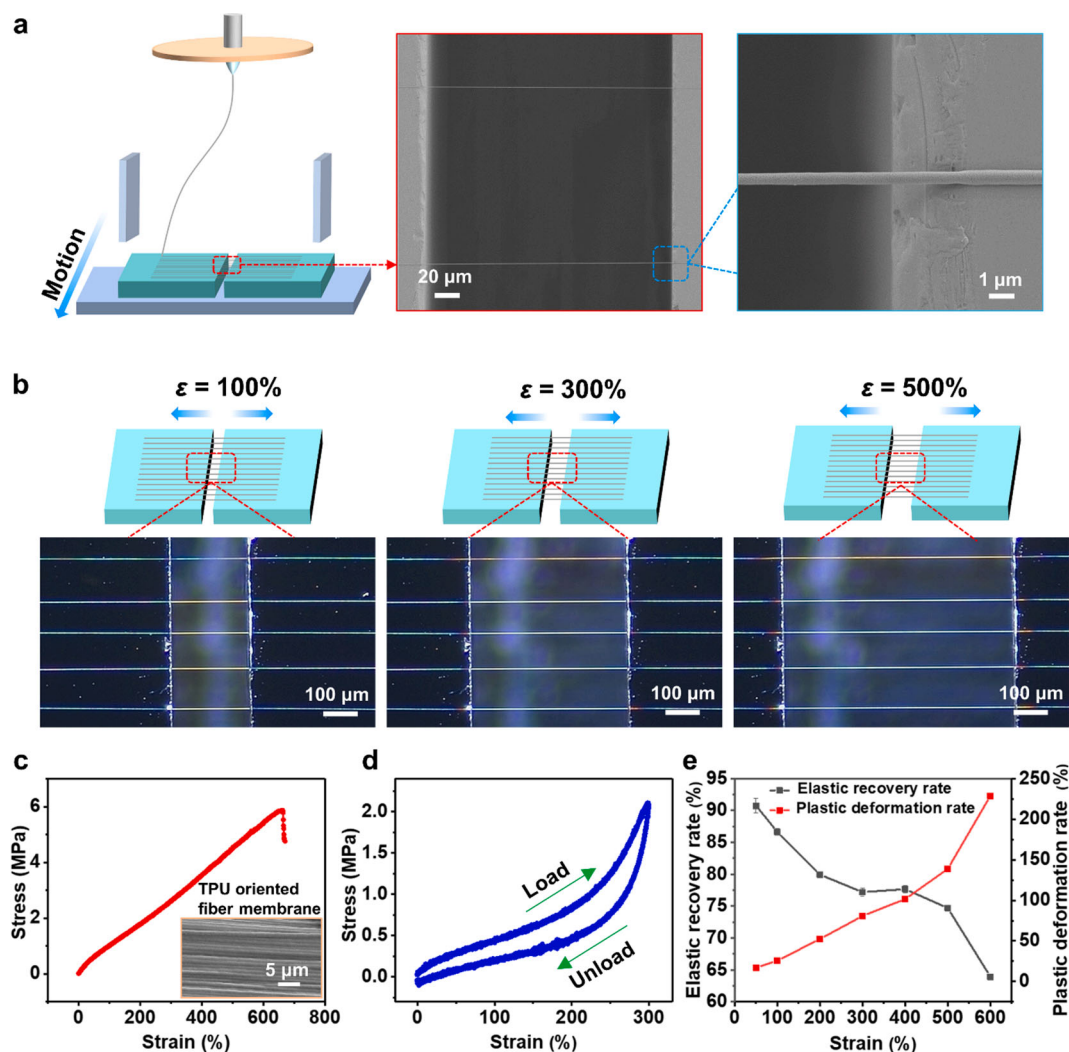


Fig. 3. Preparation and mechanical properties characterization of oriented TPU fibers: (a) Schematic diagram of oriented TPU fibers deposited on two silicon wafers and SEM images of TPU fibers. (b) Optical images of TPU fibers stretched to 100%, 300% and 500% strain respectively. (c) The tensile stress-strain curve of oriented TPU fiber membrane and corresponding SEM image. (d) 300% tensile strain, load-unload curve. (e) Elastic recovery properties of oriented TPU fibers under different tensile strains.

3.4. Preparation of pressure sensors

The preparation process of the pressure sensor is shown in Fig. 4. The pressure sensor designed in this study is mainly divided into three parts. First part is based on the Polydimethylsiloxane (PDMS) tooth structures as the substrates and electrodes of the pressure sensor. The liquid PDMS was poured into the template with the tooth-shaped domain area of 1 cm \times 1 cm (Fig. 4a), cured in a thermostat at 80 $^{\circ}\text{C}$, and then peeled off from the template, the tooth structure substrates were prepared (Fig. 4b). Then, the PDMS tooth structure substrates were placed in high vacuum magnetron sputtering coater, and the metals were deposited on the tooth structures as the electrodes. In this work, sputtered Ti (titanium) with a thickness of 10 nm on the substrate as a transition layer to increase the adhesion of the subsequent sputtering metal to the substrate, and then sputtered the thickness of 300 nm Ag (silver) on the tooth structure area as the electrodes of the capacitive pressure sensor (Fig. 4c). The SEM image of the cross section of tooth electrode after sputtering the metals is shown in Fig. 4g, in which the alveolar depth reaches $179 \pm 10 \mu\text{m}$. The second part of the sensor was to deposit a layer of oriented TPU fiber membrane (Fig. 4d) on the tooth-shaped structure substrates as the isolation layer and stress-bearing layer between the tooth-shaped structures and the polyelectrolyte membrane. In

the SEM images (Fig. 4i), the TPU fiber membrane deposited on the tooth structure can be clearly seen. The third part of the sensor is a layer of polyelectrolyte membrane prepared by PVDF-HFP mixed with LiTFSI. After depositing the oriented TPU fiber membrane on the tooth structure substrates, the prepared polyelectrolyte membrane was placed on the oriented TPU fiber membrane (Fig. 4e), and the SEM image of polyelectrolyte membrane is shown in Fig. 4h. Finally, a sandwich capacitive sensor was assembled, which composed of two PDMS tooth structure substrates, two layers of TPU oriented fiber membranes and a layer of polyelectrolyte membrane (shown in Fig. 4f).

3.5. Characterization and application

Fig. 5a is a schematic of the internal structure of the sensor when it is under different pressure conditions. The isolation effect of TPU fibers makes the sensor capacitance obtain a small initial value. When pressure is applied to the sensor, the tooth structures are close to each other, the length of the fibers becomes longer due to stretching, and the diameter becomes smaller (shown in Fig. 5b). As the diameter shrinks, gaps are created between the fibers, and the tip of the tooth structure contact with the polyelectrolyte membrane through the gaps between the TPU fibers to form electric double layers. When the pressure further

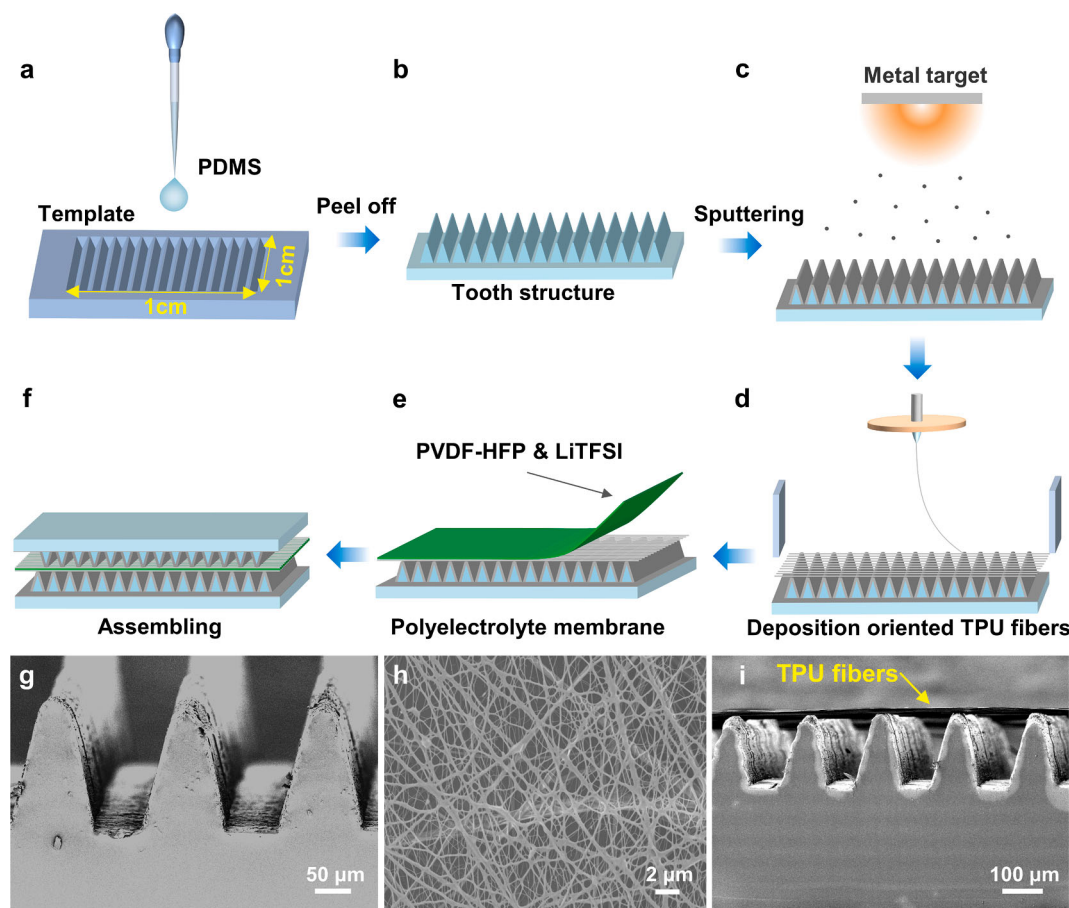


Fig. 4. Preparation of pressure sensors: (a) PDMS liquid filling template. (b) Peel off and get the tooth structure. (c) Sputtered metals (Ti and Ag) on the tooth structure as electrodes. (d) Oriented TPU fiber membrane deposited on the tooth electrode. (e) Add polyelectrolyte membrane (PVDF-HFP & LiTFSI). (f) Assembling. (g) SEM image of tooth electrode cross section. (h) SEM image of polyelectrolyte membrane. (i) SEM image of the cross section of tooth electrode with deposited oriented TPU fibers.

increases, the distance between the upper and lower tooth structures decreases, and the contact area between the tooth structures and the polyelectrolyte membrane gradually increases. At the same time, the density of polyelectrolyte membrane increases, making ions migration easier (as shown in Fig. S6, Supporting Information), and the tooth-shaped electrodes with large alveolar depth bring more sidewall surfaces contact, resulting in the expansion of electric double layer area, so that the capacitance value of the pressure sensor can continue to change greatly in a large range. Fig. 5c is the sensitivity curve of the sensor, the calculation formula of sensitivity S is as follows:

$$S = \frac{\partial(\Delta C/C_0)}{\partial P} \quad (3)$$

where $\Delta C/C_0$ is the relative change of capacitance, P represents the pressure on the sensor. Fig. 5c shows the sensitivity curve of the sensor before and after the 2000 cycles test. Before 2000-cycle test, the sensitivity of the sensor in low pressure range (0–1.1 kPa) was 42.64 kPa^{-1} , and in the medium and high pressure region (1.1 kPa–100 kPa) was 230.10 kPa^{-1} . After 2000 cycles of testing, the sensitivity of the sensor in low pressure range (0–1.1 kPa) increased to 59.84 kPa^{-1} , but in the medium and high pressure region (1.1 kPa–100 kPa) decreased to 179.07 kPa^{-1} . In addition, the sensitivity curve of the sensor without adding LiTFSI into the polyelectrolyte membrane (Fig. S7, Supporting Information) was tested, the sensitivity was 2.45 kPa^{-1} in low pressure range (less than 7 kPa), and 0.51 kPa^{-1} in the high pressure region (7–100 kPa). Fig. 5d shows the response and recovery curve of the sensor under the pressure of 100 Pa, the response time and recovery time were

within 258 ms. According to the five cycles response curves of the sensor in the low pressure region (50 Pa, 70 Pa, 100 Pa, 200 Pa and 300 Pa), the sensor could respond stably under different pressures, and the sensor also showed good response performance under the low pressure of 50 Pa, in which the $\Delta C/C_0$ value had obvious change, about 0.14 (shown in Fig. 5e). Under high pressure, the sensor could maintain a stable response for many cycles. Fig. 5f is the response curves of the sensor in the medium and high pressure region (10 kPa, 30 kPa, 50 kPa, 70 kPa, 100 kPa). In order to verify the stability of the sensor, we tested the sensor for 300 cycles under different pressures (Fig. S10, Supporting Information). Moreover, we tested 2000 cycles at the pressure of 10 kPa, and the sensor still maintained a relatively stable response (Fig. S11, Supporting Information). In the initial stage of the fatigue test, the $\Delta C/C_0$ value of the sensor was around 1500. After about 1800 cycles, the $\Delta C/C_0$ value decreased to about 1300. The influence of temperature and humidity on the sensor can not be ignored. With the temperature of the test chamber increase, more ions get rid of binding and participate in the formation of electric double layers, which increases the capacitance of the sensor. At 30°C , the value of $\Delta C/C_0$ is large, and the sensitivity reaches a higher level (Fig. S8(a)). When the set temperature is increased, the initial value of capacitance C_0 increases (Fig. S8(b)), which leads to the decrease of $\Delta C/C_0$, and the measurement curves at 50°C and 60°C nearly coincide. As shown in Fig. S9 (Supporting Information), we placed a 2 g mass on the sensor and measured the change of capacitance at 10%, 20%, 30%, 40%, 50%, 60%, 70%, 80% and 90% relative humidity, respectively. It can be seen that the capacitance gradually increases with the increase of humidity. We also tested the

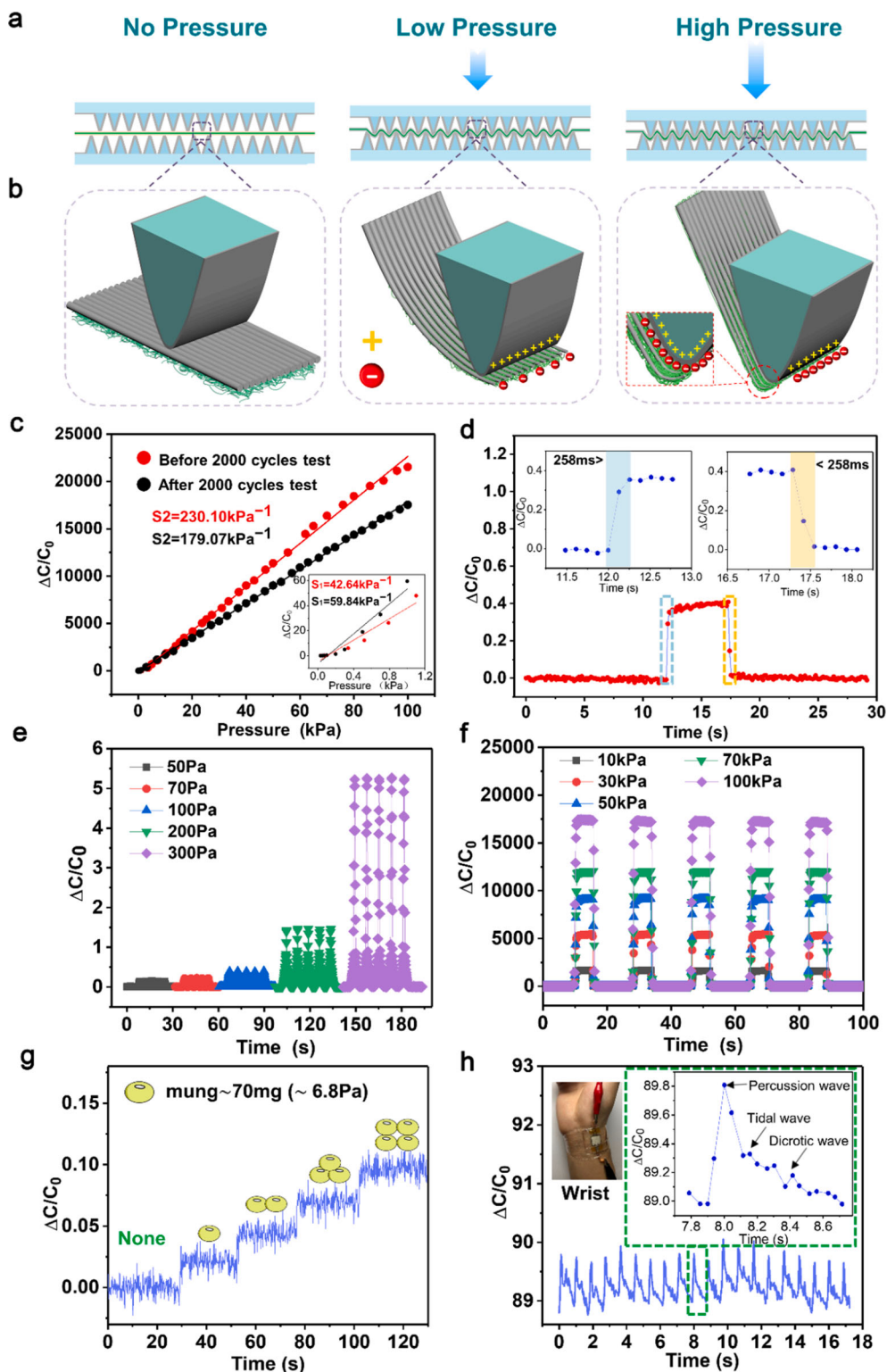


Fig. 5. Characterization and application: (a) Schematic diagram of pressure sensors under different pressure conditions, (b) the internal structure changes and the formation of electric double layer. (c) Sensitivity curve. (d) 100 Pa response time curve. (e) Low pressure region (50 Pa, 70 Pa, 100 Pa, 200 Pa and 300 Pa) response test. (f) High pressure region (10 kPa, 30 kPa, 50 kPa, 70 kPa, 100 kPa) response test. (g) Response curve of sensor to mung beans. (h) Wrist pulse wave detection and exhibit percussion wave, tidal wave and dicrotic wave.

sensor's response to tiny objects and chose mung bean as the test object. The mass of a single mung bean is about 70 mg (about 6.8 Pa), and the response curve of gradually adding mung beans to the sensor is shown in Fig. 5g. Initially, nothing was added to the sensor, and then mung beans were added one by one, and the $\Delta C/C_0$ value of the sensor changed significantly, about 0.023. When the addition of mung beans was stopped, the $\Delta C/C_0$ value measured by the sensor could maintain a stable fluctuation range. Over the years, numerous studies on pulse wave

have been reported, and human health monitoring has become a trend [41,42]. It is very interesting to apply the designed pressure sensors in practice. We applied the designed pressure sensors to the detection of human pulse wave. From the test curve (Fig. 5h), the designed sensor successfully detected the pulse wave, and could observe the weak characteristic wave signal of pulse wave, including the percussion wave (P wave), tidal wave (T wave) and dicrotic wave (D wave). Besides detecting small changes, it could also test large-scale movements, such

as straightening and bending of the knee and wrist (Fig. S12, Supporting Information). The continuous movement and state maintenance of the joint can also be detected according to the change of the $\Delta C/C_0$ value (Fig. S12 (b), Supporting Information). Compared with other reported studies (Table S1, Supporting Information), our sensors have excellent advantages in linear range (1.1–100 kPa) and sensitivity (230.10 kPa⁻¹). In the performance characterization experiment of the sensors, an LCR meter with the test voltage of 500 mV was used, and the test frequency was 300 Hz except for Fig. 5h, which was 1000 Hz to get more details of the wrist pulse wave.

4. Conclusions

In summary, we excellently realized the controllable deflection deposition of single stable jet in the far field EHD. By constructing auxiliary electric fields to constrain the jet movement, the problem of far-field EHD jet instability was solved, and the deposition of single stable jet with a collection distance of 10 cm could be easily realized. The jet motion could be controlled by adjusting the auxiliary electric fields to control the deposition of the jet. Through this method, we successfully prepared oriented fibers and printed regular grid patterns. Subsequently, we designed highly stretchable oriented TPU fiber membrane with tensile strain up to 600% as the isolation layers of the pressure sensor to control the formation of the electric double layers, and realized an ultra-broad linear range (1.1–100 kPa) with ultra-high sensitivity of 230 kPa⁻¹. In addition, the response time of the pressure sensor is less than 258 ms, and exhibits stable response characteristics for multiple cycles under different pressures. The pressure sensor can sense single mung bean with a mass of just 70 mg, and the accompanying change of $\Delta C/C_0$ is about 0.023. Practically, it can not only detect weak pulse wave characteristic signals, but also can be applied to large-scale motion monitoring such as knee joints and wrists.

Declaration of Competing Interest

The authors declare that they have no known competing financial interests or personal relationships that could have appeared to influence the work reported in this paper.

Acknowledgements

Q. Y, S. X. contributed equally to this work. This work was financially supported by the Guangdong Major Scientific Research Project (2018KZDXM061).

Appendix A. Supplementary data

Supplementary data to this article can be found online at <https://doi.org/10.1016/j.cej.2022.136370>.

References

- [1] X. Zhang, X. Jiang, Z. Zhang, H. Qin, Fabrication of silver microstructures via electrohydrodynamic inkjet printing as customizable X-ray marker in bio-structure for biomedical diagnostic imaging, *Int. J. Adv. Manuf. Technol.* 114 (2021) 241–250, <https://doi.org/10.1007/s00170-021-06858-1>.
- [2] Z. Sun, E. Zussman, A.L. Yarin, J.H. Wendorff, A. Greiner, Compound core-shell polymer nanofibers by co-electrospinning, *Adv. Mater.* 15 (2003) 1929–1932, <https://doi.org/10.1002/adma.200305136>.
- [3] D.W. Song, S.H. Kim, H.H. Kim, K.H. Lee, C.S. Ki, Y.H. Park, Multi-biofunction of antimicrobial peptide-immobilized silk fibroin nanofiber membrane: implications for wound healing, *Acta Biomater.* 39 (2016) 146–155, <https://doi.org/10.1016/j.actbio.2016.05.008>.
- [4] L. Du, X. Quan, X. Fan, G. Wei and S. Chen, Wei and S. Chen, Conductive CNT/nanofiber composite hollow fiber membranes with electrospun support layer for water purification, *J. Membr. Sci.* 596 (2020) 117613. doi: 10.1016/j.memsci.2019.117613.
- [5] R. Balgis, H. Murata, Y. Goi, T. Ogi, K. Okuyama, L. Bao, Synthesis of dual-size cellulose-polyvinylpyrrolidone nanofiber composites via one-step electrospinning method for high-performance air filter, *Langmuir* 33 (2017) 6127–6134, <https://doi.org/10.1021/acs.langmuir.7b01193>.
- [6] D. Sengupta, S.-H. Chen, A. Michael, C.Y. Kwok, S. Lim, Y. Pei, A.G.P. Kottapalli, Single and bundled carbon nanofibers as ultralightweight and flexible piezoresistive sensors, *npj Flexible, Electronics.* 4 (2020) 9, <https://doi.org/10.1038/s41528-020-0072-2>.
- [7] C. Lang, J. Fang, H. Shao, X. Ding, T. Lin, High-sensitivity acoustic sensors from nanofibre webs, *Nat Commun.* 7 (2016) 11108, <https://doi.org/10.1038/ncomms11108>.
- [8] Y.S. Park, J. Kim, J.M. Oh, S. Park, S. Cho, H. Ko, Y.K. Cho, Near-field electrospinning for three-dimensional stacked nanoarchitectures with high aspect ratios, *Nano Lett.* 20 (2020) 441–448, <https://doi.org/10.1021/acs.nanolett.9b04162>.
- [9] T. Zhang, H. Li, Z. Yang, F. Cao, L. Li, H. Chen, H. Liu, K. Xiong, J. Wu, Z. Hong, W. Wang, Electrospun YMn2O5 nanofibers: a highly catalytic activity for NO oxidation, *Appl. Catal. B Environ.* 247 (2019) 133–141, <https://doi.org/10.1016/j.apcatb.2019.02.005>.
- [10] C. Alegre, C. Busacca, A. Di Blasi, O. Di Blasi, A.S. Arico, V. Antonucci, E. Modica, V. Baglio, Electrospun carbon nanofibers loaded with spinel-type cobalt oxide as bifunctional catalysts for enhanced oxygen electrocatalysis, *J. Energy Storage* 23 (2019) 269–277, <https://doi.org/10.1016/j.est.2019.04.001>.
- [11] A. Kantürk Figen, Improved catalytic performance of metal oxide catalysts fabricated with electrospinning in ammonia borane methanolysis for hydrogen production, *Int. J. Hydrogen Energy* 44 (2019) 28451–28462, <https://doi.org/10.1016/j.ijhydene.2019.02.017>.
- [12] T.-H. Han, R. Nirmala, T.W. Kim, R. Navamathavan, H.Y. Kim, S.J. Park, Highly aligned poly(vinylidene fluoride-co-hexafluoro propylene) nanofibers via electrospinning technique, *J. Nanosci. Nanotechnol.* 16 (1) (2016) 595–600.
- [13] W. Fu, Y. Dai, X. Meng, W. Xu, J. Zhou, Z. Liu, W. Lu, S. Wang, C. Huang, Y. Sun, Electronic textiles based on aligned electrospun belt-like cellulose acetate nanofibers and graphene sheets: portable, scalable and eco-friendly strain sensor, *Nanotechnology* 30 (4) (2019) 045602.
- [14] A. Theron, E. Zussman, A.L. Yarin, Electrostatic field-assisted alignment of electrospun nanofibers, *Nanotechnology* 12 (2001) 384–390, <https://doi.org/10.1088/0957-4484/12/3/329>.
- [15] M.J. Bauer, C.S. Snyder, C.C. Bowland, A.M. Uhl, M.A.K. Budi, M. Villancio-Wolter, H.A. Sodano, J.S. Andrew, Structure-property relationships in aligned electrospun barium titanate nanofibers, *J. Am. Ceram. Soc.* 99 (2016) 3902–3908, <https://doi.org/10.1111/jace.14455>.
- [16] G.S. Bisht, G. Canton, A. Mirsepasi, L. Kulinsky, S. Oh, D. Dunn-Rankin, M. J. Madou, Controlled continuous patterning of polymeric nanofibers on three-dimensional substrates using low-voltage near-field electrospinning, *Nano Lett.* 11 (2011) 1831–1837, <https://doi.org/10.1021/nl2006164>.
- [17] D. Shin, S. Choi, J. Kim, A. Regmi, J. Chang, Direct-printing of functional nanofibers on 3D surfaces using self-aligning nanojet in near-field electrospinning, *Adv. Mater. Technol.* 5 (2020) 2000232, <https://doi.org/10.1002/admt.202000232>.
- [18] D. Sun, C. Chang, S. Li, L. Lin, Near-field electrospinning, *Nano Lett.* 6 (2006) 839–842, <https://doi.org/10.1021/nl0602701>.
- [19] D. Cho, J.S. Jang, S.H. Nam, K. Ko, W. Hwang, J.W. Jung, J. Lee, M. Choi, J. W. Hong, I.D. Kim, S. Jeon, Focused electric-field polymer writing: toward ultralarge, multistimuli-responsive membranes, *ACS Nano* 14 (2020) 12173–12183, <https://doi.org/10.1021/acsnano.0c05843>.
- [20] D. Li, Y. Wang, Y. Xia, Electrospinning of polymeric and ceramic nanofibers as uniaxially aligned arrays, *Nano Lett.* 3 (2003) 1167–1171, <https://doi.org/10.1021/nl0344256>.
- [21] Y. Song, Y. Wang, L. Xu, M. Wang, Fabrication and characterization of electrospun aligned porous PAN/Graphene composite nanofibers, *Nanomaterials (Basel)* 9 (2019) 1782, <https://doi.org/10.3390/nano9121782>.
- [22] K. Wang, H. Tan, D. Tian, B. Xiong, L. Zhang, J. Zhu, Generation of aligned electrospun fibers by using insulating and hydrophobic collectors, *ACS Appl. Polym. Mater.* 2 (2020) 2151–2159, <https://doi.org/10.1021/acscapm.0c00121>.
- [23] J. Lee, S.Y. Lee, J. Jang, Y.H. Jeong, D.W. Cho, Fabrication of patterned nanofibrous mats using direct-write electrospinning, *Langmuir* 28 (2012) 7267–7275, <https://doi.org/10.1021/la3009249>.
- [24] X. Cui, L. Li, F. Xu, Controlled assembly of poly(vinyl pyrrolidone) fibers through an electric-field-assisted electrospinning method, *Appl. Phys. A* 103 (2010) 167–172, <https://doi.org/10.1007/s00339-010-6036-y>.
- [25] C. Grasl, M.M.L. Arras, M. Stoiber, H. Bergmeister, H. Schima, Electrodynamical control of the nanofiber alignment during electrospinning, *Appl. Phys. Lett.* 102 (5) (2013) 053111, <https://doi.org/10.1063/1.4790632>.
- [26] I. Liashenko, J. Rosell-Llompart, A. Cabot, Ultrafast 3D printing with submicrometer features using electrostatic jet deflection, *Nat Commun.* 11 (2020) 753, <https://doi.org/10.1038/s41467-020-14557-w>.
- [27] I. E. Rebrov, K. I. Lukanina, T. E. Grigoriev, A. V. Bakirov, S. V. Krashennnikov, P. V. Dmitryakov, R. A. Kamyshinsky, C. G. Antipova, S. N. Chvalun and V. Y. Khomich, Enhanced electrospinning: Multi-level fiber alignment by control of electrohydrodynamic jet motion for tissue engineering, *Chem. Eng. J.* 418 (2021) 126561. <https://doi.org/10.1016/j.cej.2020.126561>.
- [28] Kyobin Keum, Jimi Eom, Jun Ho Lee, Jae Sang Heo, Sung Kyu Park, Yong-Hoon Kim, Fully-integrated wearable pressure sensor array enabled by highly sensitive textile-based capacitive ionotronic devices, *Nano Energy* 79 (2021) 105479. doi: 10.1016/j.nanoen.2020.105479.
- [29] Xin He, Zhihao Liu, Gengzhe Shen, Xiang He, Jionghong Liang, Yu Zhong, Tianlong Liang, Jie He, Yue Xin, Chi Zhang, Dongdong Ye, Guofa Cai, Microstructured capacitive sensor with broad detection range and long-term stability for human

- activity detection, *npj Flex Electron.* 5 (2021) 17. doi: 10.1038/s41528-021-00114-y.
- [30] Maeum Han, Junyeop Lee, Jae Keon Kim, Hee Kyung An, Shin-Won Kang, Daewoong Jung, Highly sensitive and flexible wearable pressure sensor with dielectric elastomer and carbon nanotube electrodes, *Sens. Actuata. A Phys.* 305 (2020) 111941.
- [31] J. Yang, S. Luo, X.i. Zhou, J. Li, F.u. Jianting, W. Yang, D. Wei, Flexible, tunable, and ultrasensitive capacitive pressure sensor with microconformal graphene electrodes, *ACS Appl. Mater. Interfaces* 11 (2019) 14997–15006, <https://doi.org/10.1021/acsami.9b02049>.
- [32] M. Li, J. Liang, X. Wang, M. Zhang, Ultra-Sensitive flexible pressure sensor based on microstructured electrode, *Sensors* 20 (2020) 371, <https://doi.org/10.3390/s20020371>.
- [33] S.G. Yoon, B.J. Park, S.T. Chang, Highly sensitive piezocapacitive sensor for detecting static and dynamic pressure using ion-gel thin films and conductive elastomeric composites, *ACS Appl. Mater. Interfaces* 9 (2017) 36206–36219, <https://doi.org/10.1021/acsami.7b11700>.
- [34] Jun Chang Yang, Jin-Oh Kim, Oh Jinwon, Se Young Kwon, Joo Yong Sim, Da Won Kim, Han Byul Choi, Steve Park, Microstructured porous pyramid-based ultrahigh sensitive pressure sensor insensitive to strain and temperature, *ACS Appl. Mater. Interfaces* 11 (21) (2019) 19472–19480.
- [35] Yongsong Luo, J. Shao, Shouren Chen, Xiaoliang Chen, Hongmiao Tian, Xiangming Li, Liang Wang, Duorui Wang, Lu Bingheng, Flexible capacitive pressure sensor enhanced by tilted micropillar arrays, *ACS Appl. Mater. Interfaces* 11 (19) (2019) 17796–17803.
- [36] Sudeep Sharma, Ashok Chhetry, Shipeng Zhang, Hyosang Yoon, Chani Park, Md Hyunsik Kim, Xue Hui Sharifuzzaman, Jae Yeong Park, Hydrogen-bond-triggered hybrid nanofibrous membrane-based wearable pressure sensor with ultrahigh sensitivity over a broad pressure range, *ACS Nano* 15 (3) (2021) 4380–4393.
- [37] G. Collins, J. Federici, Y. Imura, L.H. Catalani, Charge generation, charge transport, and residual charge in the electrospinning of polymers: a review of issues and complications, *J. Appl. Phys.* 111 (4) (2012) 044701.
- [38] L. Lin, Y. Choi, T. Chen, H. Kim, K.S. Lee, J. Kang, L. Lyu, J. Gao, Y. Piao, Superhydrophobic and wearable TPU based nanofiber strain sensor with outstanding sensitivity for high-quality body motion monitoring, *Chem. Eng. J.* 419 (2021), 129513, <https://doi.org/10.1016/j.cej.2021.129513>.
- [39] P. Mistry, R. Chhabra, S. Muke, A. Narvekar, S. Sathaye, R. Jain, P. Dandekar, Fabrication and characterization of starch-TPU based nanofibers for wound healing applications, *Mater. Sci. Eng C Mater. Biol. Appl.* 119 (2021), 111316, <https://doi.org/10.1016/j.msec.2020.111316>.
- [40] S. Choi, Y. Eom, S.-M. Kim, D.-W. Jeong, J. Han, J.M. Koo, S.Y. Hwang, J. Park, D. X. Oh, A self-healing nanofiber-based self-responsive time-temperature indicator for securing a cold-supply chain, *Adv. Mater.* 32 (11) (2020), e1907064, <https://doi.org/10.1002/adma.201907064>.
- [41] P.-Y. Zhang, H.-Y. Wang, A framework for automatic time-domain characteristic parameters extraction of human pulse signals, *EURASIP J. Adv. Signal Process.* 2007 (2008) 1–9, <https://doi.org/10.1155/2008/468390>.
- [42] C. Xia, Y. Li, J. Yan, Y. Wang, H. Yan, R. Guo and F. Li, A practical approach to wrist pulse segmentation and single-period average waveform estimation, 2008 International Conference on BioMedical Engineering and Informatics. 2 (2008) 334–338. <https://doi.org/10.1109/BMEI.2008.140>.
- [43] Y. Xiong, Y. Shen, L. Tian, Y. Hu, P. Zhu, R. Sun, C.-P. Wong, A flexible, ultra-highly sensitive and stable capacitive pressure sensor with convex microarrays for motion and health monitoring, *Nano Energy* 70 (2020), 104436, <https://doi.org/10.1016/j.nanoen.2019.104436>.
- [44] S.H. Cho, S.W. Lee, S.H. Kim, S. Chang, D. Kang, I. Hwang, H.S. Kang, B. Jeong, E. H. Kim, S.M. Cho, K.L. Kim, H. Lee, W. Shim, C. Park, Micropatterned pyramidal ionic gels for sensing broad-range pressures with high sensitivity, *ACS Appl. Mater. Interfaces* 9 (2017) 10128–10135, <https://doi.org/10.1021/acsami.7b00398>.
- [45] Shin, Y. M. Hohman, M. M. Brenner, M. P. Rutledge, G. C, Electrospinning: A whipping fluid jet generates submicron polymer fibers, *Appl Phys Lett.* 78 (2001) 1149–1151. <https://doi.org/10.1063/1.1345798>.
- [46] M.M. Hohman, M. Shin, G. Rutledge, M.P. Brenner, Electrospinning and electrically forced jets. I. Stability theory, *Phys. Fluids* 13 (2001) 2201–2220, <https://doi.org/10.1063/1.1383791>.
- [47] K. Garg, G.L. Bowlin, Electrospinning jets and nanofibrous structures, *Biomicrofluidics* 5 (2011) 13403, <https://doi.org/10.1063/1.3567097>.
- [48] K. Kang, D. Yang, J. Park, S. Kim, I. Cho, H.-H. Yang, M. Cho, S. Mousavi, K. Choi, Hyun, Park, Inkyu, Micropatterning of metal oxide nanofibers by electrohydrodynamic (EHD) printing towards highly integrated and multiplexed gas sensor applications, *Sens. Actuata. B Chem.* 250 (2017) 574–583, <https://doi.org/10.1016/j.snb.2017.04.194>.
- [49] L. Jiang, Y. Zhao, J. Zhai, A lotus-leaf-like superhydrophobic surface: a porous microsphere/nanofiber composite film prepared by electrohydrodynamics, *Angew. Chem.* 116 (33) (2004) 4438–4441.
- [50] C. Yeom, K. Chen, D. Kiriya, Z. Yu, G. Cho, A. Javey, Large-area compliant tactile sensors using printed carbon nanotube active-matrix backplanes, *Adv. Mater.* 27 (2015) 1561–1566, <https://doi.org/10.1002/adma.201404850>.
- [51] S.Y. Kim, S. Park, H.W. Park, D.H. Park, Y. Jeong, D.H. Kim, Highly sensitive and multimodal all-carbon skin sensors capable of simultaneously detecting tactile and biological stimuli, *Adv. Mater.* 27 (28) (2015) 4178–4185.
- [52] R. Moheimani, N. Aliahmad, N. Aliheidari, M. Agarwal, H. Dalir, Thermoplastic polyurethane flexible capacitive proximity sensor reinforced by CNTs for applications in the creative industries, *Sci. Rep.* 11 (2021) 1104, <https://doi.org/10.1038/s41598-020-80071-0>.
- [53] X. Sun, J. Sun, T. Li, S. Zheng, C. Wang, W. Tan, J. Zhang, C. Liu, T. Ma, Z. Qi, C. Liu, N. Xue, Flexible tactile electronic skin sensor with 3D force detection based on porous CNTs/PDMS nanocomposites, *Nano-Micro Lett.* 11 (1) (2019).